Talanta Open 6 (2022) 100144

Contents lists available at ScienceDirect

Talanta Open

journal homepage: www.sciencedirect.com/journal/talanta-open

Smart electrochemical sensing of xylitol using a combined machine learning and simulation approach

Gloria Ebube Uwaya [a], Salvador Sagrado [b,c], Krishna Bisetty [a,*]

[a] Department of Chemistry, Faculty of Applied Sciences, Durban University of Technology, Durban 4000 South Africa
[b] Departamento de Química Analítica, Universitat de València, Burjassot, Valencia E- 46100, Spain
[c] Instituto Interuniversitario de Investigación de Reconocimiento Molecular y Desarrollo Tecnológico (IDM), Universitat Politècnica de València, Universitatde València, Valencia, Spain

ARTICLE INFO

Keywords:
Electrochemical sensor
xylitol
MWCNT
gold
Monte Carlo
Density functional theory
molecular dynamics
machine learning

ABSTRACT

A novel sensor was proposed for the detection of xylitol in sugar free chewing gum using Au nanoparticles (NPs) derived from *Callistemon viminalis* leaf extract coupled with multiwalled carbon nanotubes (MWCNTs) doped onto glassy carbon electrode (GCE). In comparison to the bare GCE, the modified GCE/MWCNT/AuNPs sensor showed about 45-fold better electrochemical response to xylitol. Under the optimal conditions, the designed sensor achieved a detection limit of 9.8×10^{-6} pM for concentrations ranging from 9.9×10^{-6} to 2.9×10^{-5} pM. The practicability was tested on sugar-free sample yielding recoveries of 97–100% with RSDs of 2.83–3.33%. Machine learning (ML) was used to predict changes in voltammetric signal with changing potential over time demonstrating the fundamental knowledge of the electrochemical reaction. The performance of the Artificial Neural Network (ANN) provides good accuracy and precision in predicting the intensity (I) along with repeated ANN runs, with a mean square error (MSE) of 0.007 (± 0.002) and a determination coefficient (R^2) of 0.9992 ± 0.0006. Additionally, the interaction of xylitol on the electrode surfaces were investigated using Monte Carlo adsorption studies and 1000 ps Molecular Dynamics simulations under NVT conditions. According to the frontier molecular orbitals obtained through Density Functional Theory calculations, the reactive sites of xylitol occur at the hydroxyl group on the second carbon. Using complementary measurement techniques, this new strategy exhibits a great potential for rapid detection of xylitol in food and dental products.

1. Introduction

According to the U.S. Food and Drug Administration, xylitol, a sugar alcohol, is a globally recognized sweetener that is approved for use in food, cosmetics and dental products due to its antibacterial and anti-cariogenic characteristics [1–3]. Xylitol occurs naturally in low amounts in plants (fruits, legumes, and vegetables) and can also be obtained artificially through chemical and biotechnological processes [1,3]. As a result, xylitol is used in the treatment of diabetes, the prevention of otitis media (ear infection) in children, and for reabsorbing sugar in baked goods, candy, and chewing gum in order to prevent cavities and bad breath [1]. However, an excessive consumption of xylitol can cause osmotic diarrhoea and gastrointestinal distress [1]. Clearly, there is a need for a fast, accurate and reliable analytical tool for xylitol in food, drugs and cosmetics.

Current analytical techniques such as electrophoresis [4], chromatography [3,5] and electrochemical methods [1,6–8] are reported for the detection of xylitol. When compared with separation techniques, electrochemical assays offer the advantages of rapid analysis times, low costs, simple instrumentation, and superior sensitivity and selectivity. It has been shown that electrochemical sensors are more sensitive when modified with nanostructured materials such as metal/metal oxide nanoparticles, carbon nanotubes, polymers, quantum dots, and metal organic frameworks (MOFs) because of their large surface area and superior electron transport efficiency[9].

A growing number of sensors are being designed using metal nanomaterials. In particular, gold (Au) nanoparticles (NPs) are one of the most extensively studied noble metal nanoparticles with widespread applications in both drug delivery [10] and chemical/biosensing [9,11]. AuNPs have gained extensive attention due to their unique properties that include low toxicity, high surface to volume ratio, excellent electrical conductivity and biocompatibility [12–15]. Recently, multiwall

* Corresponding author.
E-mail address: bisettyk@dut.ac.za (K. Bisetty).

https://doi.org/10.1016/j.talo.2022.100144
Received 30 June 2022; Received in revised form 30 August 2022; Accepted 3 September 2022
Available online 5 September 2022

carbon nanotubes (MWCNTs) have gained widespread recognition as a potential component of electrochemical sensors due to their large surface area, excellent electrical conductivity, chemical stability, ability to enhance the rate of electrochemical reactions, and adhesion to electrode surfaces [11,16,17]. These carbon nanotubes such as MWCNT serve as excellent conductors for dispersion of metal nanoparticles, owing to their large surface area, which improves electron transport reactions [14]. Several studies have shown that the combination of AuNPs and MWCNT improves the conductivity and sensitivity of sensors for the detection of pesticides [9], serotonin [16] and bisphenol [11] to mention just a few. A number of existing electrochemical sensors for xylitol have been reported, including boron-doped carbon electrodes [1], polycrystalline Pt III electrodes [6], $Ni(OH)_2$/Ni electrodes[8] and poly(3-aminophenylboronic acid-reduced graphene oxide modified electrodes [7] with exception of MWCNT and AuNPs composites modified electrode. Inspired by the combination of the properties of these nanocomposites, herein we report the design of a MWCT/AuNPs based sensor for xylitol detection.

In this work, AuNPs were biosynthesized from *Callistemon viminalis* leaf extract due to its advantages over chemical synthesis, such as decreased toxicity, environmental friendliness, low cost and simplicity. Although Kumar et al. (2011), reported on AuNPs synthesised from *Callistemon viminalis* leaf extract, there is no report on the detection of analytes [18]. Thus, we investigated the electrocatalytic activity of the electrode modification materials towards xylitol in this study.

Amongst the recognized statistical techniques, artificial neural networks (ANN) can be a useful method for modelling electrochemical data/response [19]. Literature reports the application of ANN in signal modelling or processing of biosensors for catechol, glutamic acid, organophosphate, and electrochemical sensor response for maleic hydrazide [19–22]. ANN methodology falls into ML or artificial intelligence approaches, and it is capable of modelling complex, linear and non-linear relationships between input (predictor) and outputs (response) variable(s) [19,23,24]. The ANN performance can depend on the neurons/layer's architecture, the initial values of inner weights and the validation (to control overfitting) and test (as independent 'external' data to the ANN) subsets, as well as the activation functions (to modulate the data transfer between neurons). In the feed-forward mode, all the cells (neurons) in the layers are interconnected by inner weights (to be optimised during the training stage). The architecture must guarantee good performance, lack of overfitting (i.e., comparable quality for training, validation and test outputs) and reliability (low uncertainty in replicated runs). Novel quality indicators are designed to control all these aspects.

However, the point of using ML is to analyse and make a prediction for a complicated system, such as voltammetric signal changing over time, yielding fundamental knowledge of the system. Thus, another objective of this work was to combine the developed electrochemical sensor with ANN (an ML model) as an intelligent data analysis and smart transformation for digital output of xylitol, aimed at estimating the Intensity (I) at a given potential (V), oxidation or reduction phase (pH) and scan rate (SC) from the available CV data (scan rate variation) of xylitol.

Finally, the electronic properties of xylitol were assessed by density functional theory (DFT) calculations, while the interactions between xylitol and the nanostructured modified electrode surfaces and binding energies were investigated by Monte Carlo (MC) and molecular dynamics (MD) simulations respectively. This combined study could open a synergic pathway to expand the design of healthy sweeteners.

2. Materials and methods

2.1. Reagents and chemicals

Gold (III) chloride hydrate ($HAuCl_4$), xylitol ($C_5H_{12}O_5$), and multi-walled carbon nanotubes (MWCNTs) were acquired from sigma Aldrich, potassium ferricyanide and ferrocyanide trihydrate ($K_3Fe(CN)_6$ and $K_4Fe(CN)_6{\cdot}3H_2O$), anhydrous mono sodium hydrogen orthophosphate (NaH_2PO_4) and di-sodium hydrogen orthophosphate (NaH_2PO_4) were procured from associated chemical enterprises. Dimethylformamide (DMF) from RADCHEM. Phosphate buffer solution (0.1 M, pH 5) was prepared by mixing appropriate amount of 0.1 M mono sodium hydrogen orthophosphate (NaH_2PO_4) and 0.1 M di-sodium hydrogen orthophosphate. A 5 mM $[Fe(CN)_6]^{3-/4-}$ solution was prepared using suitable mass of $K_3Fe(CN)_6$ and $K_4Fe(CN)_6{\cdot}3H_2O$ in PBS. Analytical grade reagents were used in this work and solutions were prepared using deionized water (DW).

2.2. Preparation of extract, AuNPs and nanocomposite (MWCNT/Au)

Callistemon viminalis leaf extract was prepared by dispersing 2.5 g of dried ground leaves in 100 mL DW while stirring and boiling for 20 min at 85 °C. The mixture was cooled and filtered. AuNPs was synthesized by boiling 100 mL of 1 mM $HAuCl_4$ for 10 min at 90 °C, followed by the addition of leaf extract (80 mL) under stirring at room temperature for 24 h. The reduction of Au^{3+} to Au^0 was noticed by the colour transformation from yellow to deep purple on adding *C. viminalis* leaf extract, confirming the formation of AuNPs [25,26]. The nanoparticles were washed three times with DW by centrifugation, and oven dried overnight at 90 °C. A mixture of MWCNT and AuNPs was prepared by dispersing 6 mg MWCNT into 250 μL of DMF, followed by the addition of 12 mg AuNPs. After stirring for 30 min, the mixture was dried at 50 °C for 3 h to evaporate the solvent.

2.3. Characterization of AuNPs, MWCNT and MWCNT/AuNPs

Functional groups present in the nanomaterials (AuNPs, MWCNT and MWCNT/AuNPs) were investigated by fourier transform infrared spectroscopy. The Raman spectra were acquired with a Witec Confocal Raman Microscope (alpha300) using a 532 nm laser, while the UV–vis spectra were obtained on a Carry 60 UV–VIS of Agilent technology to study. Their surface morphology was studied on field emission scanning electron microscopy (FESEM) using the Tescan MIRA SEM, while the energy dispersive X-ray spectra (EDX) were acquired using the Thermo Fisher Nova NanoSEM, with an OxfordX-max 20 mm^2 detector and INCA software. The shape and size of formed AuNPs was obtained by transmission electron microscopy (TEM) and image J, accordingly. Electrochemical characterization was performed by cyclic voltammetry (CV) and electrochemical impedance spectroscopy (EIS).

2.4. Preparation of real samples

A xylitol containing sugar-free gum (Stimorol) was acquired from a local supermarket and pulverized using a mortar and pestle, with 10 mL PBS. The extraction procedure was repeated three times in 25 mL PBS. The extracts were filtered to remove particulates and thereafter refrigerated prior to DPV analysis. PBS could possibly dissolve the xylitol in the chewing gum fully since the analytical grade xylitol was highly soluble in PBS at a physiological pH. Also, previous study reports the use of deionized water for extraction [3] with a pH close to PBS. Since the study was not aimed at a quantitative determination of total xylitol in chewing gum, there was no experiment performed to ensure that xylitol was fully extracted from the chewing gum.

2.5. Fabrication of GCE/MWCNTs/AuNPs

The GCE was polished in a slurry of alumina powder, cleaned in DW, and then cleaned in methanol (50%) and oven dried at 50 °C for 2 min before modification. Approximately 0.25 μL of homogeneous paste of MWCNT and AuNPs was dropped onto a cleaned GCE, followed by drying in a 50 °C oven for 2 min to yield GCE/MWCNT/AuNPs. Both GCE/AuNPs and GCE/MWCNT were modified using separate suspensions of 3 mg AuNPs and MWCNT following the same steps as GCE/

MWCNT/AuNPs. Scheme 1 illustrates the fabrication of the designed sensor.

2.6. Electrochemical set up

Electrochemical measurements were performed using the Metrohm Autolab (PGSTAT 302 with FRA 32) workstation in a three-electrode system. The bare and modified glassy carbon electrodes (GCE of 3 mm diameter, GCE/AuNPs, GCE/MWCNT, and GCE/MWCNT/AuNPs) were applied as working electrodes, platinum, and silver/silver chloride (Ag/AgCl) saturated in 3 M potassium chloride as auxiliary and reference electrodes, respectively. Electrochemical behaviour of 0.01 M xylitol using bare GCE, and modified electrodes were carried out by CV from 0 to 1.2 V potential window at a scan rate of 25 mV/s, start and stop potential (0.0 V), upper vertex potential (1.2), lower vertex potential (0.0 V) and step potential of 0.00244 V in 0.1 M PBS containing 0.01 M xylitol. On the other hand, the interfacial properties of the electrodes were investigated by EIS with frequency range of 100 kHz – 0.1 Hz at fixed potential (1 V) for GCE, GCE/AuNPs and GCE/MWCNT/AuNPs and 0 V for GCE/MWCNT. Quantitative detection of xylitol was performed by DPV at a potential window of 0.4 – 1.2 V, 0.025 V modulation amplitude, with 0.05 s modulation time, 0.005 V step potential, interval of 0.5 s, scan rate of 0.01 V/s and a deposition potential of −0.8 V. Selectivity studies were conducted by chronoamperometry assays at intervals of 40 s. All electrochemical experiments were performed at room temperature.

2.7. ANN structure and nomenclature

To develop the ANN processes, some "Deep Learning Toolbox" functions (MATLAB® R2019a; Mathworks, 2022) were used. A full description of all of them is available at the supplier site (https://es.mathworks.com/help/deeplearning/referencelist.html). The main available function from the toolbox is the *feedforwardnet.m*. It generates a feed-forward (regression-focused) ANN able to approximate an unknown function (f) of the type: output $= f$ [input]; in our case, a non-linear regression predictive model: $I = f$ [V, pH, SC], to be approximated/modelled from the available data. Thus, for fixing the ANN architecture, the *feedorwardnet.m* algorithm (with default properties) was used. It consists of 3 input variables (V, pH, SC) set as the input layer and the predicted values (I) set as the output layer. ANN outputs can vary depending on the complexity of the ANN architecture, but also on the initial values and validation and test subsets, although such influence should decrease for large datasets. In this case, every single cyclic voltammogram contains 980 potential (and intensity) values, totalling 7840 data sets after joining the 8 scans at different scan rates. This number seems to be large enough to obtain adequate results starting from a random selection of initial weights values and validation and test subset (the default option), at least with a proper ANN architecture (to be optimised). In addition, the data scale is quite homogeneous and probably data normalization could be unnecessary. In the middle, we arranged up to 2 hidden layers and tried up to 30 neurons (in one or two layers). The ANN architecture was identified by 3-[NN—NN2]−1, where NN and NN2 are the number of neurons in the first and second hidden layer, respectively (NN + NN2 = 30). For training the ANN model, the *train.m* algorithm (with default properties) was used, using the available CV data. The trained ANN minimises the differences (MSE) between predicted and experimental I data. The learning stage stops after 1000 iterations (epochs) or when 6 consecutively increasing MSE values for the validation subset are reached (Fig. S1).

For each independent ANN tested, data were automatically divided (*dividerand.m* function), in a random way, into training (70%), validation (15%) and test (15%) subsets. Validation aims to control the overfitting (stopping the training) while test data (not used to build the ANN) evaluate the expected future performance of the trained ANN with novel (external) data. To compare the performance, overfitting level and uncertainty of the ANN models and summarize the results, a novel quality indicator pQ (Eq. (1)) was introduced (associated with Nr independent outputs). In each Nr-replicate, the statistic Q (Eq. (2)) is calculated, and from the Nr Q values, the mean(Q) and standard deviation, std(Q), are calculated (to be used in Eq. (1)). Q depend on two indicators (Qr and Qe; Eqs. (3) and (4), respectively). Qr is the mean of 4 regression meta parameters (for all, training, validation and test data subsets). Each Regression meta parameters (Rm; Eq. (5)) involve the R^2, slope (b_1) and intercept (b_0) from the validation plot (I estimated vs. I experimental). Qe is also the mean of 4 MSE values (all-, training-,

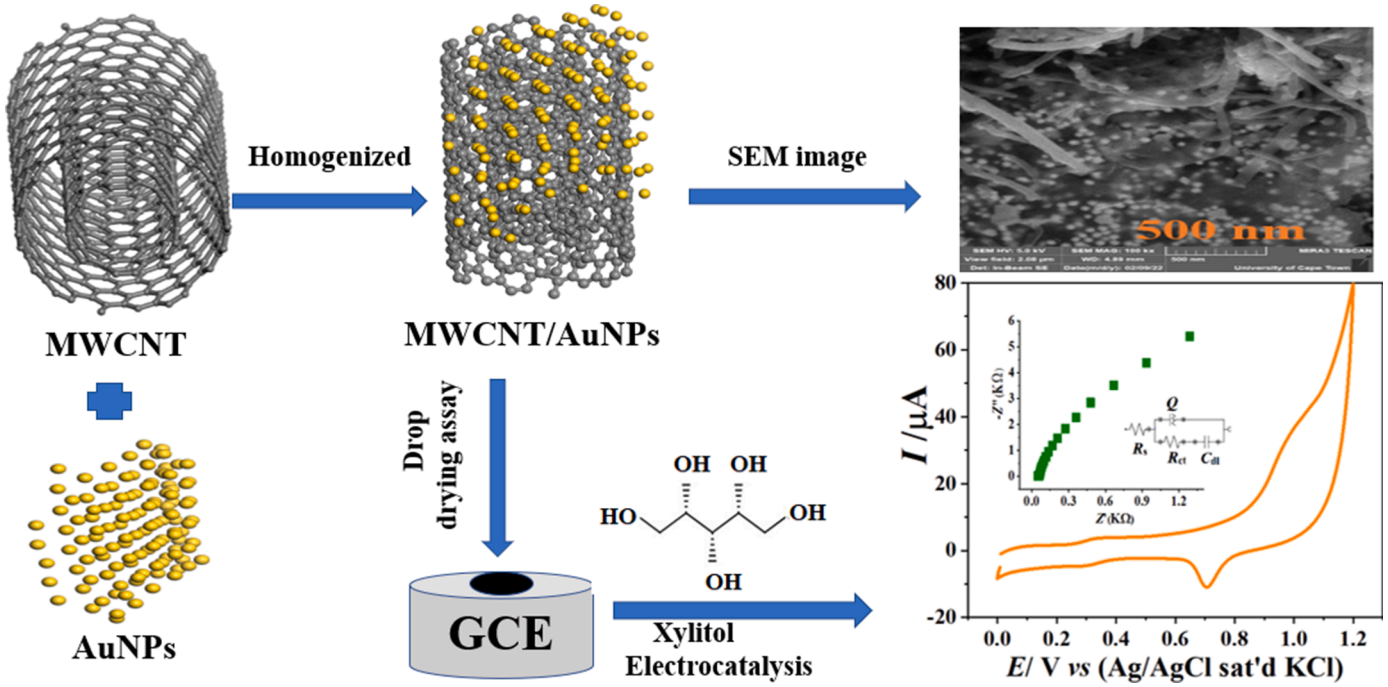

Scheme 1. Illustration of the fabrication of GCE/MWCNT/AuNPs.

validation- and test-MSE values).

$$pQ = \text{mean}(Q) - \text{std}(Q) \quad (1)$$

$$Q = Qr - Qe \quad (2)$$

$$Qr = \text{mean}(Rm) \quad (3)$$

$$Qe = \text{mean}(MSE) \quad (4)$$

$$Rm = 1 - \left(\left|1 - R^2\right| + |1 - b_1| + |b_0|\right)/3 \quad (5)$$

All these statistics involve a comparison between the estimated and experimental I value, but they control different aspects of quality. Rm resembles a conventional R^2-term (evaluating the correlation) but that is penalised when the slope or the intercepts differ from its target values, 1 and 0, respectively. In an ideal situation (i.e., $R^2 = 1$, $b_1 = 1$ and $b_0 = 0$) Rm becomes 1. Also, Q can be seen as an overall regression quality (Qr; ideally close to 1), which is penalised by overall error quality (Qe; ideally close to 0). Finally, pQ is the mean of replicated Q values, penalised by their uncertainty (standard deviation), so it accounts for the robustness of the ANN when varying their conditions (i.e., initial inner weights and subsets, randomly selected by the algorithms).

2.8. Computational methodology

2.8.1. Density functional theory (DFT) calculations

DFT calculations were performed to assess the parameters that describe the chemical reactivity of the optimized xylitol molecule. The 3D structure of xylitol was obtained from PubChem database, optimized geometrically with B3LYP density functional and 6–311+*G* basis set using the Gaussian 09 package [27]. Frequency calculations were performed to further confirm the global minimum energy for the optimized geometry. The highest occupied molecular orbital (HOMO), lowest unoccupied molecular orbital (LUMO) and the energy band gap (Eg) were visualized using GaussView 6.0 program. [28].

2.8.2. Monte Carlo and molecular dynamics simulations

A Monte Carlo (MC) adsorption analysis was applied to find the lowest energy configuration of the adsorbate (xylitol) on the surface of the substrate (GCE, GCE/AuNPs, GCE/MWCNT and GCE/MWCNT/AuNPs) by simulating the experimental electrodes. MC simulations were conducted with the Adsorption Locator (AL) module of Material Studio 2020 software [29] as previously reported [30]. The simulations were performed using a graphite surface to mimic the GCE electrode, AuNPs cleaved along the 111 plane and MWCNTs.

We then used molecular dynamics (MD) simulations to model the GCE/MWCNTs/AuNPs-xylitol system, in order to determine the binding affinity of xylitol to these materials. The MD simulations were performed in the canonical ensemble at constant temperature, volume and number of atoms (NVT) for a simulation time of 1000 ps at 1 fs time step. The temperature was controlled using the Berendsen thermostat, which is part of the Forcite module in Material Studio 2020 [26].

3. Results and discussion

3.1. Structural and morphological characterization

Fig. 1A presents the Raman spectra of AuNPs, MWCNT and MWCNT/AuNPs with prominent peaks at 1343, 1573 and 2678 cm^{-1} corresponding to the D (linked to the presence of defective carbon), G (represents pure graphite with Sp^2 carbon) and G' (first D overtone mode) band accordingly [31,32]. The D and G band was noticed at 1462 and 1525 cm^{-1} in AuNPs: 1344 and 1573 cm^{-1} for MWCNT and 1340, 1569 cm^{-1} for MWCNT/AuNPs spectra, accordingly. The peaks at 482, 1770, 2945 and 3417 cm^{-1} relates to Au nanoparticles, C=O stretching mode of carbonyl group, O—H of the carboxylic acid and alcohol groups respectively. The disappearance of the C=O peak and the appearance the O—H groups (asterisked) in MWCNT/AuNPs spectrum suggest the attachment of AuNPs on MWCNT. The intensities, a slight shift of the D and G bands to a lower and higher wave number and the structural changes observed between AuNPs and MWCNT/AuNPs spectrum, suggest the occurrence of chemical interaction between AuNPs and MWCNT. Moreover, it confirms the successful decoration of MWCNT surfaces with Au nanoparticles. Crystallinity was determined from the relative intensity of D/G (I_D/I_G) of Au (0.95), MWCNT (0.8540) and MWCNT/AuNPs (0.8540), suggesting a reasonable crystallinity.

The IR spectra of the electrode modification materials are depicted by Fig. 1B. Characteristics peaks at 568, 1211 and 1731cm^{-1} representing AuNPs, C—N and carbonyl group stretch (C=O) was noticed in AuNPs spectrum. Similar peaks are noticeable in the spectrum of the nanocomposites (MWCNT/AuNPs), although with slight shift for the C=O band and the appearance of some new bands at 1455 and 2837 cm^{-1} assigned to CH_3 and C—H stretch which are absent in the MWCNT spectrum. The observations confirmed the attachment of AuNPs on MWCNT.

The reduction of gold ion (Au^{3+}) to its zero valent state (Au^0) was further verified from the UV–vis spectrum scanned in the range of 300 – 800 nm (Fig. 1C). Characteristic absorption peak for AuNPs was noticed at 541 nm, corresponding to the surface resonance plasma [25,26] and close to the absorption band (543 nm) reported in literature [25]. Fig. 1C shows the UV–vis spectrum of the nanocomposite (MWCNT/AuNPs) with noticeable absorption peak at 537 nm. The slight shift to a lower wavelength (hypsochromic shift) connotes the occurrence of interaction between MWCNT and AuNPs.

Fig. 1D-F shows the FE-SEM images of AuNPs, MWCNT, and MWCNT/AuNPs composite respectively. From Fig. 1D, a well dispersed spherical shaped AuNPs is noticed. MWCNT image (Fig. 1E) shows the presence of entangled fibres while the morphology of the nanocomposite in Fig. 1F clearly reveals the attachment of AuNPs to the MWCNT surface confirmed by the presence of white spots [9,14,15,33]. Additionally, there is an intertwined web visible which could explain the electrochemical sensing and electrical conductivity properties of the nanocomposite [14].

The elemental composition of AuNPs, MWCNT, and MWCNT/AuNPs has been verified by EDS analysis. Fig. 1G-I demonstrate the presence of gold (Au), carbon (C) and oxygen (O). The emission of O and C atoms on the spectrum of Au nanoparticles could possibly have resulted from leaf extract and the EDX grid, respectively.

TEM study was conducted to understand the shape and size of the biosynthesized AuNPs. The TEM image presented by Fig. 1J depicts some hexagonal, nearly spherical, spherical and a triangular shaped AuNPs, similar to a study in literature [25]. Particle size distribution was estimated to be 29.97 nm with a mean size and standard deviation (δ) of 11.22 and 4.06, respectively using Image J software (Fig. 1K). The found size is within the range reported in literature (5 – 30 nm) [25]

3.2. Electrochemical characterization of the modified GCEs

The electrochemical performance of the bare and modified electrodes (GCE, GCE/AuNPs, GCE/MWCNT and GCE/MWCNT/AuNPs) was investigated using CV and EIS in a redox probe of $[Fe(CN)_6]^{3-/4-}$ (prepared in 0.1 M PBS as supporting electrolyte). Fig. 2A shows the CV responses at the electrodes at scan rate of 25 mV/s with an amplified peak current noticed at GCE/MWCNT/AuNPs in contrast to other electrodes. Redox peaks were observed at all the electrodes. GCE/MWCNT/AuNPs displayed a greater peak current in contrast to other electrodes, suggesting an excellent electrocatalytic activity. This was ascribed to a rapid electron transport rate, confirmed by the active surface area estimated using Eq. (7). The number of electrons transferred at each electrode was approximately 1 using Eq. (6). The calculated active surface area for all the electrodes in an ascending order is $5.6 \times 10^{-5} < 9.8 \times 10^{-4} < 2.6 \times 10^{-3} < 3.7 \times 10^{-3}$ cm^2 for GCE/AuNPs, GCE, GCE/

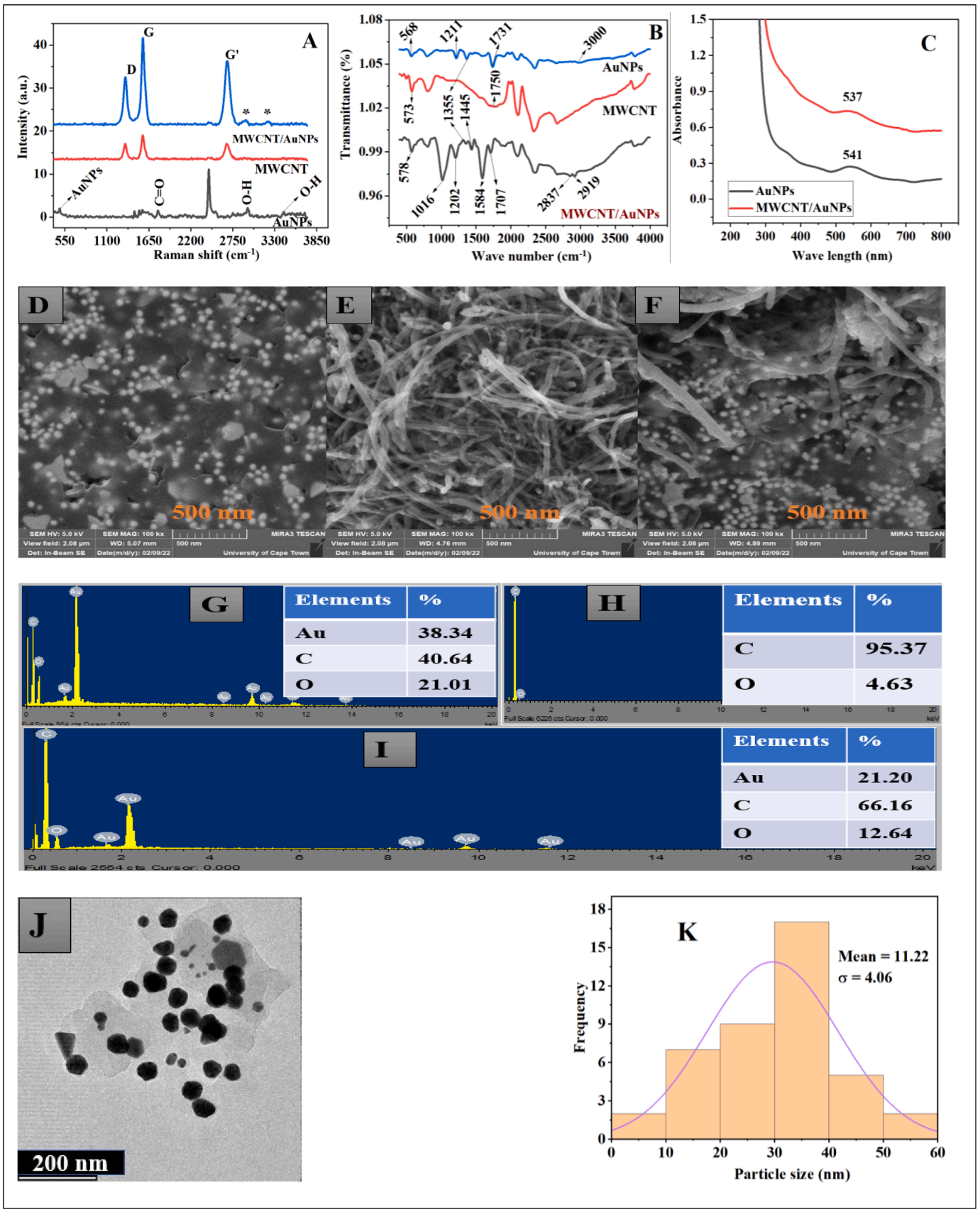

Fig. 1. Raman (A), FTIR (B), UV–Vis (C) SEM images (D, E, F), and EDS spectra (G, H, I) for AuNPs, MWCNT and MWCNT/AuNPs and TEM image (J) and particles size distribution (K) for AuNPs.

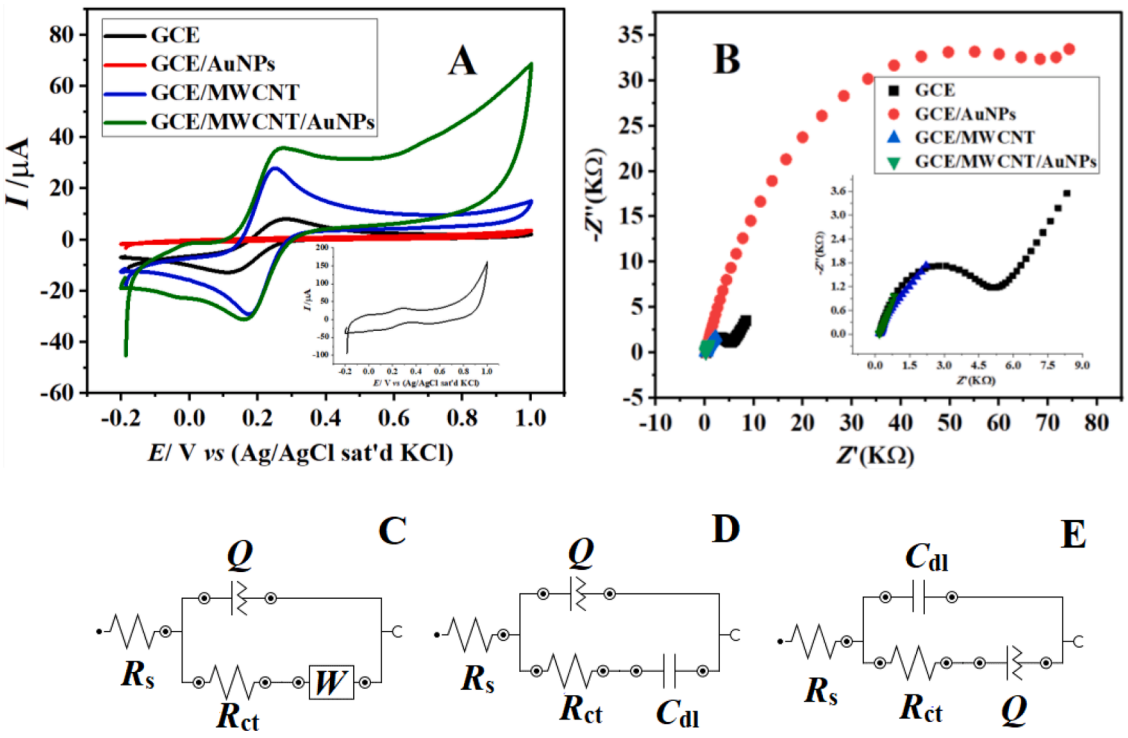

Fig. 2. (A) Cyclic voltammogram at scan rate of 25 mV/s and (B) Nyquist spectra of bare GCE and modified electrode in 5 mM $[Fe(CN)_6]^{3-/4-}$ prepared in PBS, pH 7. Insert of A is CV on GCE/MWCNT/AuNPs in PBS only while insert of B is CV of GCE, GCE/MWCNT and GCE/MWCNT/AuNPs in 5 mM $[Fe(CN)_6]^{3-/4-}$ (C -E) Circuit models applied in the fitting of EIS data.

MWCNT and GCE/MWCNT/AuNPs respectively. The peak observed at about −0.01 V on GCE/MWCNT/AuNPs could probably have resulted from the PBS which is obvious in the insert of Fig. 2A.

$$\Delta E = \frac{2.303RT}{n} \tag{6}$$

$$I_p = \left(2.69 \times 10^5\right) n^{3/2} A C D^{1/2} V^{1/2} \tag{7}$$

Where, ΔE, R, and T represents the peak potential separation, gas constant and temperature accordingly while I_p, n, *A D, C* and *V* represents the peak current (amperes), number of electrons transferred, surface area of the electrode in cm^2, concentration of $[Fe(CN)_6]^{3-/4-}$ solution in mol/cm^3 and *v* is the scan rate in V/s, accordingly.

EIS was conducted to examine the electron transfer properties of various modified electrodes in the presence of $[Fe(CN)_6]^{3-/4-}$ redox probe. Fig. 2B presents the Nyquist spectra for all the electrodes while the equivalent circuits employed in the fitting of EIS data are shown in Fig. 2C (GCE), D (GCE/AuNPs and GCE/MWCNT) and E (GCE/MWCNT/AuNPs). Where R_s, R_{ct}, *Q, W* and C_{dl} represents the solution resistance, charge transfer resistance, constant phase element, Warburg (semicircle-infinite straight line, relating to electron transfer diffusion of the redox probe at the electrode surface), and double layer capacitance accordingly. R_{ct} values of 4791, 9778, 0.137 and 0.048 KΩ were obtained at GCE, GCE/AuNPs, GCE/MWCNT and GCE/MWCNT/AuNPs, respectively. The high R_{ct} value observed at GCE/AuNPs in contrast to bare GCE electrode suggest resistance to electron transport which could be linked to decreased surface area. The lowest R_{ct} value recorded at the GCE/MWCNT/AuNPs electrode could be linked to the synergies of the electrical conductivity of AuNPs and MWCNT with increasing surface area, accelerating more electron transport between the electrolytes and the electrode surfaces. The result supports the amplified current response displayed at GCE/MWCNT/AuNPs.

The effect of varying scan rates ranging from 25 to 350 mV/s on the kinetics of the GCE/MWCNT/AuNPs electrode surface towards the electrochemical redox reaction of the probe solution was conducted using CV as shown in Fig. S2A. The CVs displayed an increase in redox peak currents with increasing scan rates. A shift in redox peak potential (anodic and cathodic peak potential to a more positive and negative region respectively) was observed with an increasing scan rate, suggesting an efficient mass transport between the electrodes [34]. Fig. S2B presents a linearly increasing peak currents with square root of scan rates ($v^{1/2}$) at the electrode, demonstrating that the redox process at the nanocomposite modified electrode surface is diffusion-controlled [15]. This was further confirmed by the graph of log of peak currents (I_p) versus log *v* (Fig. S2C) which yielded a slope (< 1) which is expected for an ideal diffusion controlled electrode reaction [15,35]. Fig. S2D shows the plot of Ep against logarithm of scan rate (*v*), yielding two straight lines with slopes - $\frac{2.303RT}{\alpha nF}$ and $\frac{2.303RT}{(1-\alpha)nF}$ corresponding to cathodic and anodic peaks respectively [36,37]. The apparent charge transfer coefficient (α) and the number of electrons (n) involve in the oxidation/reduction of $[Fe(CN)_6]^{3-/4-}$ ions at the surface of the electrode were 0.54 and 0.908 respectively [37]. Also, the electron transfer rate (ks) was estimated as 0.83 s^{-1} based on Eq. (8).

$$\log ks = \alpha\log(1-\alpha) + (1-\alpha)\log\alpha \; - \; \log\frac{RT}{nFv} - \alpha(1-\alpha)\frac{nF\Delta E_p}{2.3RT} \tag{8}$$

3.3. Electrochemical detection of xylitol

3.3.1. Effect of pH and deposition potential

To illustrate that the peak current of analyte depends strongly on supporting electrolyte pH and deposition potential, the current response of xylitol was investigated in different pHs and deposition potentials on the nanocomposite modified electrode (GCE/MWCNT/AuNPs). The effect of solution pH on the peak currents (I_{pa}) of 0.01 M xylitol in 0.1 M PBS was investigated within a pH range of 5–8 which are still closer to physiological pH as presented in Fig. S3A. The oxidation peak current for xylitol was only noticed at pH 5 in contrast to literature [1], suggesting that levels of catalysis sensitivity of analyte in different pH media differs with electrode modification materials. Therefore pH 5 was

employed throughout the experiment. The effect of deposition potential was studied using DPV from −0.8 to 0.4 V in 0.01 M xylitol. Based on the maximum peak current observed at −0.8 V (Fig. S3B), the deposition potential was subsequently set at −0.8 V.

3.3.2. *Electrochemical behaviour of xylitol*

The electrochemical behaviour of xylitol on the bare and modified electrodes (GCE, GCE/AuNPs, GCE/MWCNT and GCE/MWCNT/AuNPs) was investigated by CV and EIS (Fig. 3A and C). Fig. 3B is the cv response in the presence and absence of 0.01 M xylitol in 0.1 M PBS. From Fig. 3A, xylitol displayed an irreversible oxidation reaction, except for GCE/MWCMT, which exhibited a capacitive current. The absence of a peak for xylitol oxidation could be attributed to the accumulation of xylitol ions on the MWCNT surface controlled by the electric double layer capacitance (EDLC) [38,39]. This demonstrate the absence of ion exchange between MWCNT surface and the analyte, leading to the electrostatic electric charge storage [38]. Similar behaviour was reported in literature for the sensing of dopamine (DA) on MWCNT modified glassy carbon electrode surface (GCE-MWCNT) [40]. Oxidation peak potentials and currents were noticed at 0.90 V; 0.78 μA (bare GCE); 1.08 V; 4.20 μA (GCE/AuNPs), and 0.99 V; 34.84 μA (GCE/MWCNT/AuNPs). A peak (0.74 V) observed at the reverse scan for the GCE/MWCNT/AuNPs electrode was assigned to AuNPs. The oxidation peak current of GCE/MWCNT/AuNPs was 45 times higher than the bare GCE, suggesting an excellent electron transport and an enhanced electrocatalytic capability of AuNPs by MWCNT.

The interfacial characteristics and charge transfer properties of the bare GCE and modified electrodes were examined using an electrochemical impedance spectroscopy (EIS). Fig. 3C shows the Nyquist spectra for the electrodes in 0.01 M xylitol over a 100 kHz and 0.1 Hz frequency range at fixed applied potential of 1.0 V. The equivalent circuit models applied in the fitting are presented in Fig. 3D and E. Table 1 shows the fitting parameters and their circuit description while the estimated errors in parenthesis and the chi squares (χ^2) confirmed successful fitting of the EIS data. The values for n, indicates the behaviour of Q as a capacitor depends on the homogeneity of the electrode surface [30]. The n values for all the electrodes were < 1, implying a pseudo capacitive behaviour of the electrode-electrolyte interface towards xylitol electro-oxidation. The lowest R_{ct} value was recorded at the nanocomposite electrode (GCE/MWCNT/AuNPs), indicating a fast electron transport process resulting from an enhanced electrocatalytic effect at the electrode due to the synergies between MWCNT and AuNPs.

Table 1
Impedance data obtained for the bare and modified electrodes in 0.01 M xylitol at a constant potential of 1 V.

Electrodes	R_s (Ω)	R_{ct} (KΩ)	C_{dl} (μF)	Y (μΩ*S^{n})	n	$\chi^2 \times 10^{-1}$
GCE	62.7 (4.6)	1.38 (12.5)	0.21 (8.3)	3.09 (2.5)	0.70 (0.5)	3.4
GCE/Au	87.3 (2.4)	0.45 (6.3)	16.9 (46.0)	2.67 (2.6)	0.78 (0.5)	2.9
GCE/MWCNT	48.9 (1.0)	0.029 (20.0)	128.0 (10.1)	166 (11.2)	0.89 (1.4)	1.4
GCE/ MWCNT/ AuNPs	68.4 (1.0)	0.017 (42.6)	92.3 (28.7)	242 (11.2)	0.90 (1.4)	1.7

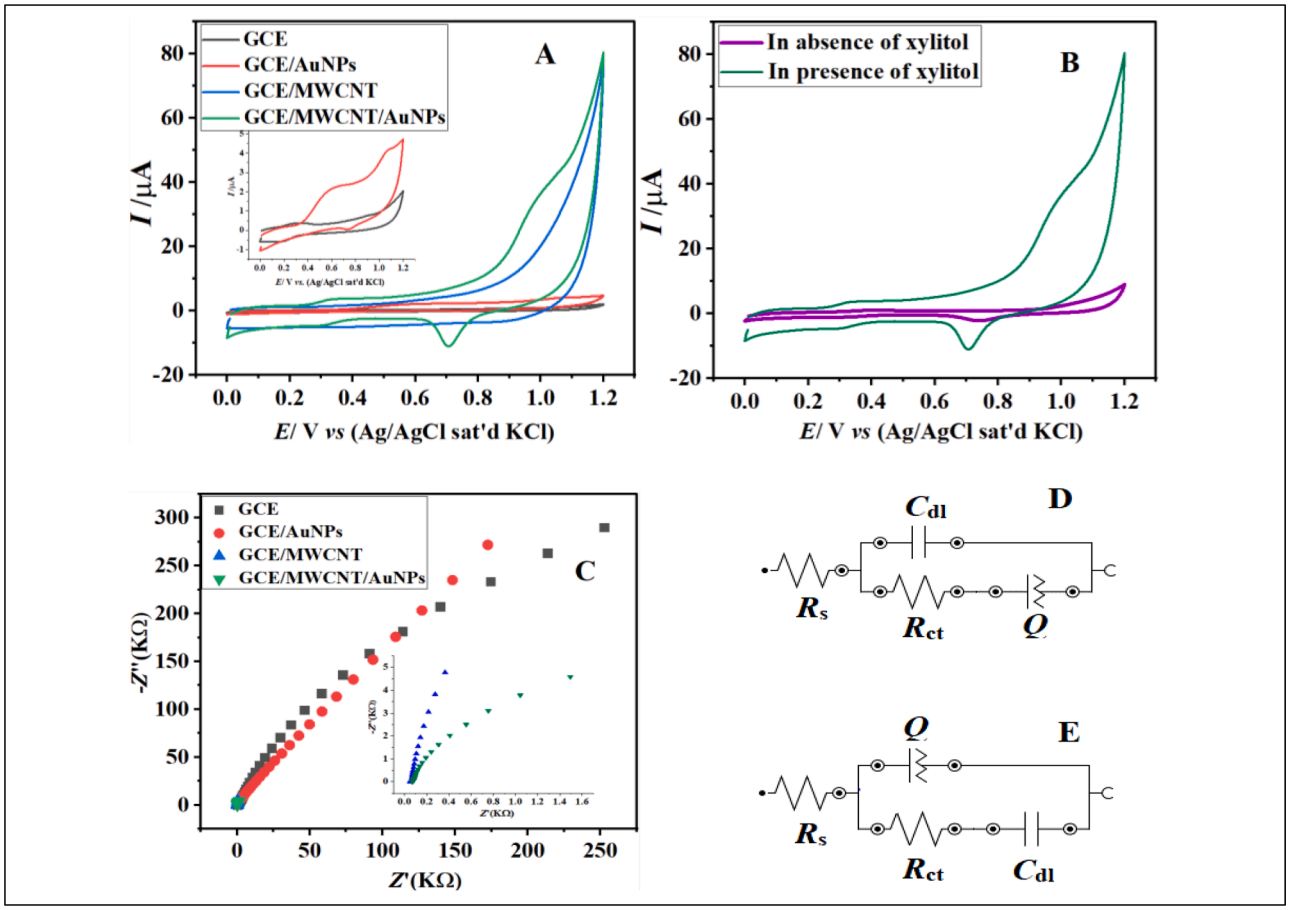

Fig. 3. (A) CVs of bare GCE and modified electrodes, insert of A are CV responses of GCE (in black) and GCE/AuNPs (in red) (B) CV of GCE/MWCNT/AuNPs in PBS with and without xylitol (C) Nyquist spectra of electrodes in 0.01 M xylitol. Equivalent circuits for electrode (D) GCE, GCE/AuNPs, GCE/MWCNT and (E) GCE/MWCNT/AuNPs.

The reduced C_{dl} value on GCE/MWCNT/AuNPs (as shown in Table 1) in comparison with GCE/MWCNT could be due to lesser charge accumulation with the presence of AuNPs.

3.3.3. Effect of scan rate

The effect of scan rate on the electrochemical oxidation of xylitol on GCE/MWCNT/AuNPs, was examined from the scan rate variation, studied in the range of 10 – 50 mV/s by CV in 0.01 M xylitol (Fig. 4A). From Fig. 4A, the peak currents increased while the peak potentials shifted to a more positive region with increasing scan rates. A linear regression value of 0.99 was observed for the plot of peak current with the square root of scan rates (Fig. 4B), demonstrating the electrochemical oxidation of xylitol on the electrode to be diffusion controlled. The plot of log I_p versus log v (Fig. 4C) yielded a slope value of 0.39 closer to 0.5 for an ideal diffusion controlled process, further supporting a diffusion-controlled reaction [1]. Diffusion coefficient and surface coverage concentration of xylitol was estimated to be 1.08 × 10^{-5} cm^2/s and 1.03 × 10^{-3} mol/cm^2 respectively from slope of Fig 4B and D, using Eqs. (9) and (10), respectively.

$$I_p = \left(2.999 \times 10^5\right) n[1-\propto]n]^{1/2} ACD^{1/2} v^{1/2} \tag{9}$$

$$I_p = \frac{n^2 F^2 A \Gamma v}{4RT} \tag{10}$$

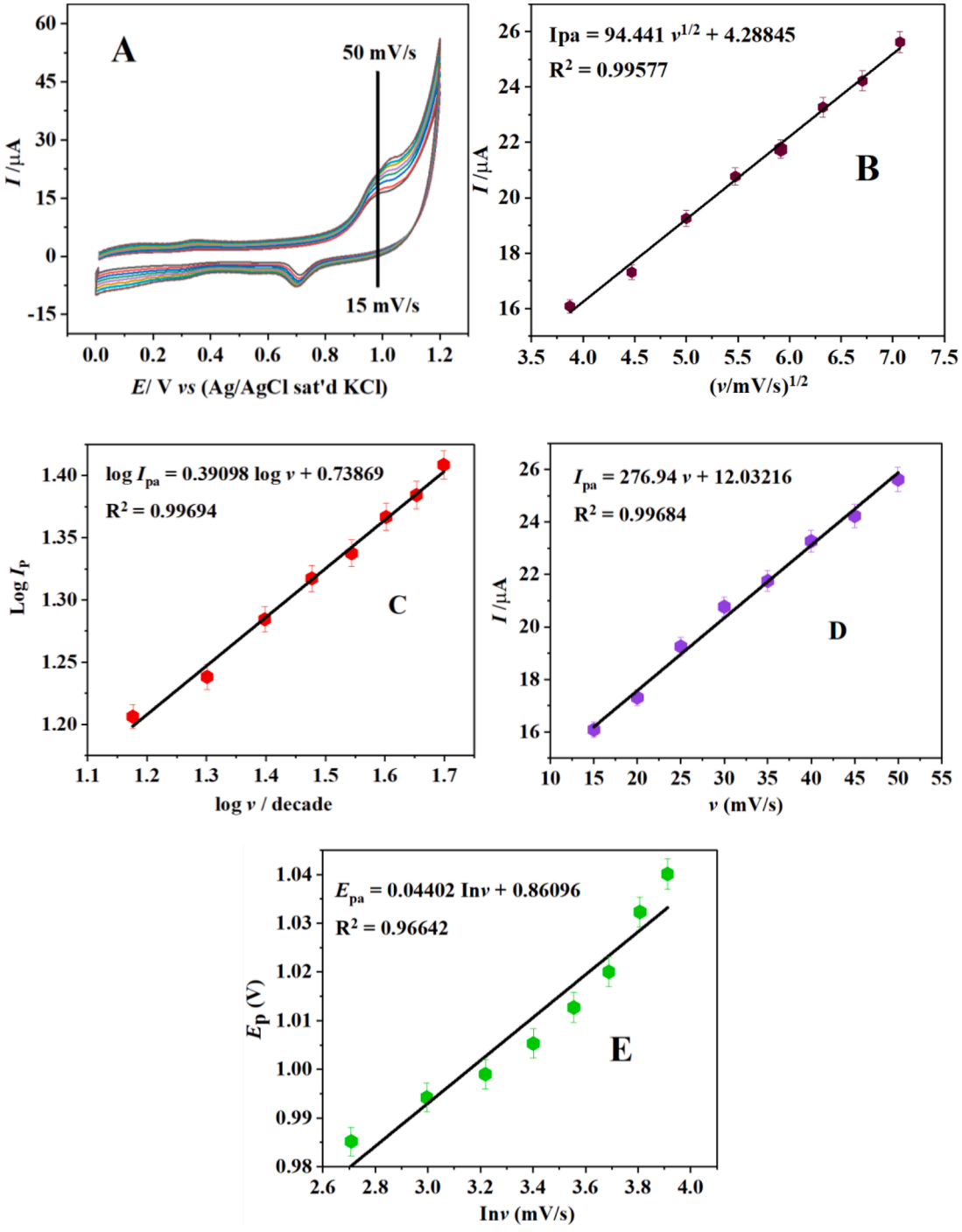

Fig. 4. CV of GCE/MWCNT/AuNPs electrode at varied scan rates (15, 20, 25, 30, 35, 40, 45 and 50 mV/s) in 0.01 M xylitol (A). Linear relation between (B) I_{pa} vs $v^{1/2}$ (C) log I_{pa} vs log v (D) I_{pa} vs v; (E) E_{pa} vs Inv.

The number of electrons (n) and α, n involve in xylitol electro-oxidation at the electrode was determined from the slope of Fig. 4E (graph of peak potential-Ep versus natural logarithm of *v*). The standard deviation error value from the linear graph was calculated to be 1.65%. The observed values for α and n were found to be 0.27 and 1.85 (approximately 2) on applying Eq. (11) [41] and 12 respectively.

$$E_p - E_{p/2} = \frac{1.857RT}{\propto F} = \propto = \frac{47.7}{E_p - E_{p/2}}\ \text{mV} \quad (11)$$

$$E_p = \frac{2.3RT}{(1-\propto)nF} \quad (12)$$

With the electronic densities of xylitol predicted HOMO-LUMO frontiers obtained by DFT calculations (Fig. 6B) and literature reporting the possibility of xylitol oxidation occurring at the hydroxyl group on Carbon 2 or 4 [1], the electrochemical oxidation mechanism of xylitol on the designed sensor (GCE/MWCMT/AuNPs) was proposed (Scheme 2).

3.3.4. Quantitative detection of xylitol

Fig. 5A shows the DPV responses recorded for quantitative detection of xylitol in PBS over concentrations ranging from 9.9×10^{-6} to 2.9×10^{-5} pM (9.9×10^{-18} to 2.9×10^{-17} M). The result shows a decrease in oxidation peak currents with increasing concentrations of xylitol. The observed decrease in xylitol DPV peak as concentration increased could be attributed to electrochemical fouling resulting from the blockage of the electrode surfaces (electrode passivation) possibly by the analyte under study (xylitol) or its reaction products [42–44], leading to decrease in active surface area which in turn reduces the sensitivity of the electrode, and the peak current. Literature also report the decrease in peak current with increasing concentration of xylitol on a PAPBA-RGO modified electrode [7]. Relative standard deviation (RSD) of 0.21 and 15.86% was recorded for peak potential and peak current accordingly. The Limit of detection (LOD) and quantification (LOQ) was computed from the calibration curve (Fig. 5B) using the following relationships $\text{LOD} = \frac{3.3\ \text{Standard deviation}}{\text{Slope}}$ and $\text{LOQ} = \frac{10\ \text{Standard deviation}}{\text{Slope}}$. The calculated LOD and LOQ were 9.8×10^{-6} and 2.97×10^{-5} pM respectively. The comparison of the obtained LOD with LOQs of other methods reported in literatures is presented in Table 2.

3.3.5. Repeatability, reproducibility, storage stability and interference study

Repeatability of GCE/MWCNT/AuNPs was measured by 10 successive CV scans in 0.1 M PBS containing 0.01 M xylitol at a scan rate of 25 mV/s. A 33.2% drop in oxidation peak current of xylitol was observed with a stronger oxidation peak (Fig. S4A). This could be ascribed to electrode fouling. RSD value of 4.2% was estimated for reproducibility studies conducted using three independent nanocomposite modified electrodes in the same xylitol concentration, demonstrating good reproducibility of the developed sensor for xylitol detection (Fig. S4B). Additionally, interference studies on the selectivity of the electrode for (ascorbic acid =AA, aspartame = AS and silymarin= SM) towards xylitol was tested by chronoamperometry at interval of 40 s. The choice of these analytes was based on the fact that AA, AS co-exist with xylitol in sugar free gum, SM regulates the sugar levels while sorbitol on the other hand was included due to a similarity in structure. Fig. S4C presents the variation of xylitol (XY) oxidation signal of the interfering species in 0.1 M PBS at pH 5. The result shows signals for xylitol after the injection of interfering species, suggesting selectivity of the electrode. In addition, storage stability of the electrode was examined using DPV in 0.01 M xylitol for 17 days with the electrode stored dried when not in use. A resulting 80% response of xylitol initial current was obtained.

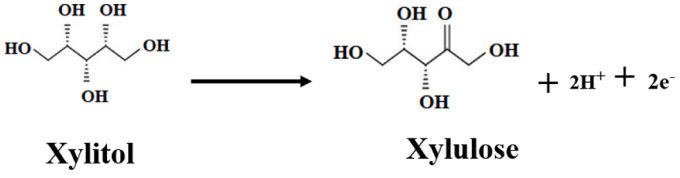

Scheme 2. Proposed electro- oxidation mechanism of xylitol.

3.3.6. Real sample analysis

To demonstrate the analytical application of the designed sensor, xylitol was detected in extracts of sugar free gum sample by standard addition method using DPV under optimal conditions. Table 3 presents the summary of the obtained results. The designed sensor yielded a reasonable standard deviation ranging from 2.83 to 3.33% with excellent recoveries in the range 97 –100%.

3.4. ANN results

3.4.1. ANN architecture optimisation

The ANN models approach a function of type $I = f$ [V, pH, SC] through a complex network of interconnected neurons (and weights and activation functions). In this study, a maximum of 30 neurons was considered. The ANN architecture was optimized by comparing Nr independent replicates (and calculating the pQ statistic, Eq. (5)) for different architectures varying the number of neurons (NN and NN2). Fig. S5A shows the pQ values for the initial study (NN: 1–20). As can be seen, the ANN architecture has a notable influence on the quality of the ANN outputs. Simpler architectures (low NN values) have lower pQ values (even negative), which are due to high MSE values and/or strange punctual results, increasing the uncertainty in Eq. (1)). The provisional conclusion was that the NN should be 15 or higher when using a single hidden layer. Accordingly, a second study was performed for NN = 15, 20, 25 and 30 neurons (Fig. S6B). As can be seen, there is an improvement when using 25 or 30 neurons. To guarantee proper robustness, with high performance (pQ close to 1), 30 neurons were finally selected for further studies. Since a parallel study using auto scaled input variables yielded similar results, the original input (or output) data were used. Due to the high pQ, expected outputs are almost independent of the starting conditions (initial inner weights; subsets) for training the ANN.

The addition of a second hidden layer could be a way to better modelling non-linearities (intrinsic to I vs. V relationships in the CV). Thus, 30 neurons were distributed into two hidden layers, from NN = 1 and NN2 = 20, and increasing NN and decreasing NN2 up to NN = 30 (NN2 = 0; tested previously), totalling 30 different architectures (15 replications for each). The results were irregular. 17 architectures provided one or more cases (replicates) where MSE (all data) was above 1 (ANN unstable). 6 architectures showed pQ values below 0.99. Thus, the reduction of the number of neurons to less than 30 was discharged. Only 7 architectures (including the case NN = 30) showed pQ > 0.99 results (Table 4). As can be seen, the architectures 3-[6–24]−1, 3-[7–23]−1, 3-[8–22]−1, 3-[9–21]−1, 3-[10–20]−1 and 3-[15–15]−1, provided slightly better (but comparable) statistics to those from the previously tested 3-[30]−1. These results correspond to the last architecture although the other in Table 4 may also be adequate.

3.4.2. Performance of the ANN (predictive ability)

Fig. 5 illustrates the I vs V data (8 scans) obtained with the single hidden layer-ANN (3-[30]−1), including only the outputs for the test data. Since they act as external data, that do not participate in either the training or the validation procedures, their performance defines the quality of the ANN in predicting new I-values (the most critical quality aspect). They are plotted over the full experimental data (dotted cyclic voltammograms). The corresponding validation plot (I predicted versus I experimental; inside plot) is also included. According to the high pQ value found, there was a good agreement between experimental and predicted values, thus validating the ANN model. There is also a good agreement between the test outputs and the target (diagonal) line.

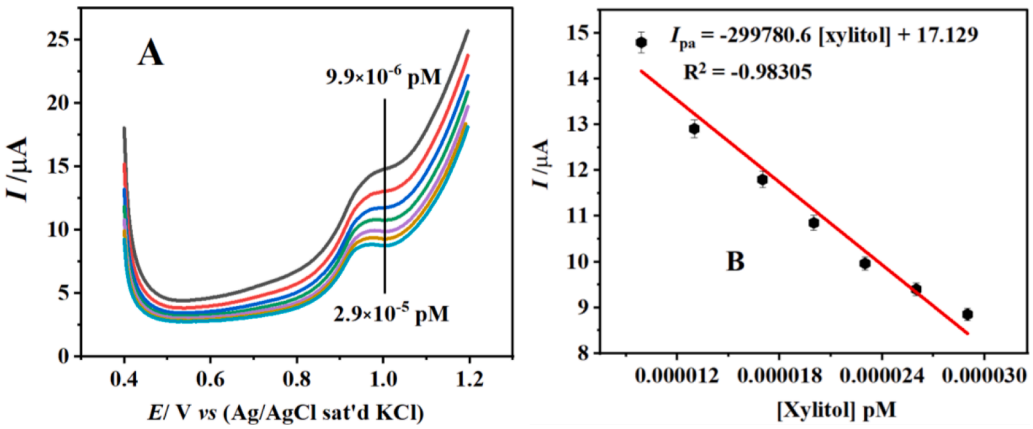

Fig. 5. DPVs at GCE/MWCNT/AuNPs in 0.1 M PBS containing different xylitol concentrations (9.9×10^{-6} to 2.9×10^{-5} pM (A) and (B) Linear relationship of the peak current response xylitol concentrations.

Table 2
Comparison of the designed sensor with literature.

Methods	Electrodes	Peak potential (V)	Supporting electrolyte	Linearity	LOD	LOQ	Regression	Ref
CV	Au	0.8	0.1 M $HClO_4$	NR	NR	NR	NR	[6]
CV	Pt (III)	0.71, 0.75	0.1 M $HClO_4$	$1 \times 10^{-3} - 3 \times 10^{-1}$ M	NR	NR	NR	[6]
SWV	B-DDE	1.8, 2.1	0.1 M PBS, pH 7	$5 \times 10^{-6} - 64 \times 10^{-6}$ M	1.3×10^{-6} mol L^{-1}	4.5×10^{-6} mol L^{-1}	0.990	[1]
DPV	PAAB-RGO/GCE			$1 \times 10^{-12} - 1 \times 10^{-2}$ M	1×10^{-13} M	NR	NR	[7]
Chronoamperometry	$Ni(OH)_2$/Ni	0.59	0.1 M NaOH	0.625–3.333 mM	29.3 μM	NR	0.990	[8]
LC-ELSD	N/A	N/A	N/A	50 – 1003 μg/mL	3.82 μg/mL	12.72 μg/mL	0.9993	[5]
LC-ESI-MS/MS	N/A	N/A	N/A	1.008 – 1008 μg/mL	0.06 μg/mL	0.19 μg/mL	0.9967	[5]
GC_MS	N/A	N/A	N/A	1.032 –1032 μg/mL	0.53 μg/mL	1.76 μg/mL	0.9978	[5]
GC–MS	N/A	N/A	N/A	0.7 – 2.0 mg/mL	0.1 mg/ mL	0.7 mg/ mL	0.9995	[3]
DPV	GCE/MWCNT/ AuNPs	0.99	PBS, pH 5	$9.9 \times 10^{-6} - 2.9 \times 10^{-5}$ pM	9.8×10^{-6} pM	2.9×10^{-5} pM	0.9769	Present study

Note: NR = Not reported; N/*A* = Not applicable.

Table 3
The detection of xylitol in sugar free gum at the designed sensor.

Serial Number	Amount added (pM)	Amount detected (pM)	Recovery (%)	RSD (%)*n* = 3
1	4.76×10^{-6}	4.71×10^{-6}	98.9	2.92
2	8.25×10^{-6}	8.23×10^{-6}	99.7	2.83
3	1.15×10^{-5}	1.08×10^{-5}	93.9	2.85
4	1.45×10^{-5}	1.40×10^{-5}	96.5	3.33

Additionally, residuals are within a range of ± 0.5 μA. Equivalent results were obtained for the rest of the subsets (not shown). These results fit well with the aim of the present study.

3.5. Computational results

3.5.1. DFT calculations

According to the HOMO-isosurface plot (Fig. 6B), the electron densities are concentrated around the five hydroxyl groups, with some contribution from the carbon and hydrogen atoms. As can be seen in Fig. 6B, the main electron density in the LUMO plot is dominated by the second hydroxyl group of the tridentate ligand ($(H—C\text{-}OH)_3$) with some contributions arising from the hydrogen atoms situated at carbon atoms 1 and 4. In addition, HOMO −1 showed electron localization mostly at the hydroxyl groups with a minor contribution from the hydroxyl group on carbon 2, while LUMO +1 showed a dense delocalization at the hydroxyl group on carbon 4. According to the electron densities, the hydroxyl groups of the xylitol molecule are the active sites. The energy bandgap values corresponding to HOMO-LUMO; HOMO −1 and LUMO +1 are −6.955 and −7.295 eV respectively, using the relation $\Delta Eg = E_{LUMO} - E_{HUMO}$, This connotes that xylitol is chemically reactive and stable.

3.5.2. Monte Carlo adsorption studies

In the present Monte Carlo (MC) analysis, the surface configurations of the optimized xylitol-substrate interactions are presented in Fig S6 A-

Table 4
ANN architecture study (15 replicates per ANN) showing those architectures with 30 neurons (arranged in one or two hidden layers) with pQ (Eq. (1)) > 0.99.

NN	NN2	pQ	Q (mean	± std)	max(Q)	min(Q)	Range(Q)	MSE>1 cases
6	24	0.9959	0.9968	0.0009	0.9979	0.9950	0.0029	0
7	23	0.9959	0.9968	0.0009	0.9979	0.9950	0.0029	0
8	22	0.9962	0.9972	0.0010	0.9980	0.9938	0.0042	0
9	21	0.9973	0.9977	0.0004	0.9983	0.9969	0.0014	0
10	20	0.9962	0.9974	0.0012	0.9981	0.9933	0.0048	0
15	15	0.9972	0.9978	0.0006	0.9984	0.9960	0.0024	0
30	–	0.9904	0.9929	0.0025	0.9958	0.9876	0.0082	0

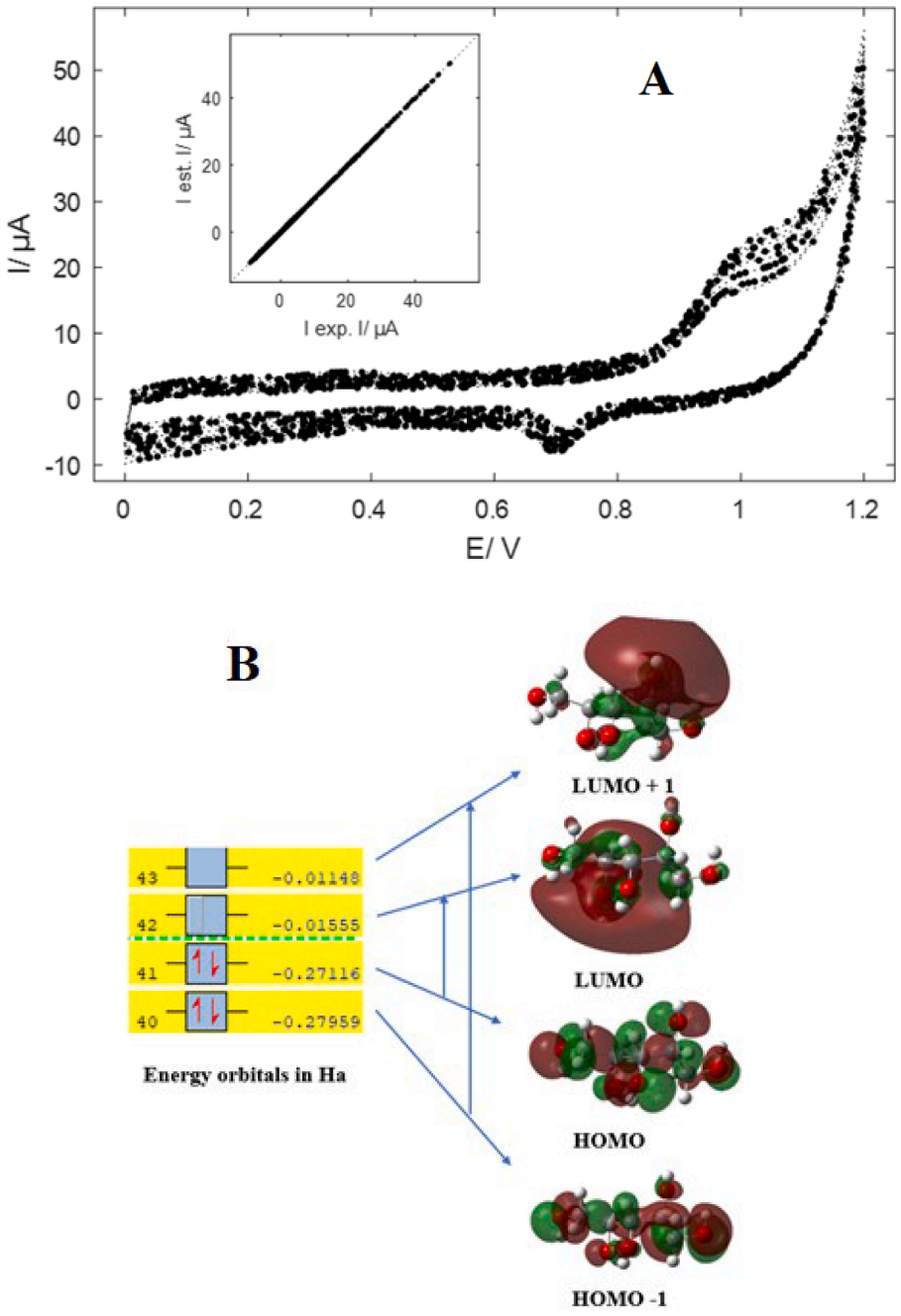

Fig. 6. (A) Performance of a 3- [30]−1 ANN model. Cyclic voltamograms (dotted line for experimental data; dots for estimated I values for the test subset) and validation plot (inside plot) for test subset (the diagonal dotted line represents the target line). (B) HOMO and LUMO plots for xylitol at B3LYP/6–311+*G* level (B).

D. It is clear from these 3D images, that xylitol is attracted to the flat surface of the GCE. In contrast, the AuNPs have a stronger affinity to the outer wall of the MWCNTs than to the bare GCE surface, thus contributing to a greater stabilization of the GCE/MWCNT/AuNPs-xylitol interaction. These findings were further confirmed by the calculated adsorption energies (E_{ads}) based on the following equation:

$$E_{ads} = E_{adsorbate} + E_{surface} - E_{adsorbates/surface}$$

where, $E_{adsorbate}$ is the adsorbate energy in the absence of the surface (substrates), $E_{surface}$ is the surface energy of the unmodified or modified electrodes and $E_{adsorbates/surface}$ is the total energy of the substrates (surface) and the adsorbate. In Table 5, the adsorption energies are all negative, indicating stabilization with strong and attractive adsorbate-substrate interactions [45,46]. GCE/MWCNT/AuNPs-xylitol results showed better stabilization and interaction with xylitol in comparison to GCE/AuNPs-xylitol, as shown by a more negative E_{ads} result, which can be attributed to the presence of MWCNTs. The observed trends for

Table 5
Summary of xylitol interactions on the mimicked electrode surfaces using MC and MD simulations.

Substrate-Adsorbate	Monte Carlo adsorption energies kcal/mol	Binding interaction energy kcal/mol
GCE	−29.982	−0.565
GCE/AuNPs	−30.128	−0.787
GCE/MWCNT	−35.646	−6.648
GCE/MWCNT/AuNPs	−36.315	−12.852

adsorption energies follows the sequence: GCE-xylitol < GCE /AuNPs-xylitol < GCE/MWCNT-xylitol < GCE/MWCNT/AuNPs-xylitol.

3.5.3. Molecular dynamics calculations

To explain the interactions between the substrate (GCE/MWCNT/AuNPs) and the adsorbate (xylitol), molecular dynamics (MD) simulations for the different substrate-adsorbate systems were implemented. As can be seen in Fig. S7A-B, the stability of the GCE/MWCNT/AuNPs-xylitol system was investigated by observing the kinetic energy and the temperature (298 K, mimicking experimental conditions) across the system. Both profiles showed steady fluctuations with no significant changes, indicating a stable temperature and kinetic energy during MD simulations [47]. Table 5 presents the binding interaction energies (E_b) derived from MD trajectories of the different substrate-adsorbate systems as calculated by the equation:

$$E_b = E_{tot} - (E_{substrate} + E_{adsorbate})$$

where, E_{tot} is the total energy of each separate system plus the interaction energy between the substrate energy ($E_{substrate}$) and the adsorbate energy ($E_{adsorbate}$). The $E_{substrate}$ was calculated as follows: after optimum configuration of the substrate-adsorbate complex was determined using MD, the adsorbate was removed from the system and a single point energy calculation was applied. Thereafter, a similar protocol was applied to the adsorbate molecule in the absence of the substrate. The trends for E_b are similar to those described above for adsorption energies. It has been reported that an electrode surface's bond strength is defined here as the degree to which an atom-bonding orbital electron is free to participate in the adsorbate (xylitol) and the electrodes [47]. The GCE/MWCNT/AuNPs exhibited the lowest binding energy (more highly negative) towards xylitol, demonstrating a stronger GCE/MWCNT/AuNPs-xylitol interaction.

3.6. Comparison of computational and experimental result

Theoretical calculations of xylitol were performed using DFT to obtain molecular orbitals (HOMO-LUMO) which determined the active site, thereby supporting the proposed mechanism for the electrode processes involving the oxidation of xylitol to xylulose. According to Fig. 3C and Table 2, R_{ct} values obtained from fitting of EIS data were lower at the nanocomposite modified electrode (GCE/MWCNT/AuNPs), indicating enhanced electron transfer properties and high electronic conductivity between MWCNT and AuNPs. A similar trend observed in the MC adsorption energies (see Table 5): GCE-xylitol < GCE/AuNPs-xylitol < GCE/MWCNT-xylitol < GCE/MWCNT/AuNPs-xylitol, suggesting the presence of MWCNT's contribution to the stronger interaction and stabilization. A low binding energy (the highly negative) was obtained for the GCE/MWCNT/AuNPs-xylitol and therefore it might be expected that the oxidation of xylitol may be adsorption controlled. It also further supports the presence of MWCNT's contribution to the lower binding energy with stronger interaction and lesser resistance to electron transfer [45,48].

4. Conclusion

A novel electrochemical sensor based on the merits of GCE/MWCNT/AuNPs was successfully fabricated for the detection of xylitol. The structural, morphological, electrocatalytic, and sensing properties of GCE/MWCNT/AuNPs toward xylitol were investigated. Compared to other electrodes studied (GCE, GCE/MWCNT, and GCE/AuNPs), the nanocomposite modified electrode demonstrated excellent electrocatalytic activity with an amplified current response and a lower charge transfer resistance. This sensor demonstrated good sensitivity, repeatability, reproducibility, and practical applicability with satisfactory recoveries and RSDs. Although the designed sensor showed narrow scan rate for xylitol, other results suggest potential application for sensing of xylitol in food and pharmaceuticals at picomolar levels. Based on the potential (V), the oxidation phase (pH) and the scan rate (SC), ANN have been used to estimate the intensity (I) of cyclic voltammograms at various scan rates. In the ANN comparison, the key is a novel 8-parameter quality indicator (pQ) that uses penalised effects (overfitting and uncertainty) based on several regression and MSE statistics. A single hidden layer-ANN architecture (3-[30]−1), after selecting the optimum architecture, offers good general performance (e.g., pQ = 0.99; MSE > 0.007 or $R^2 > 0.999$, comparable across all, training, validation and test data) in predicting I.

In addition, the DFT results revealed the hydroxyl group on the second carbon as an active site for the electrochemical oxidation of xylitol on GCE/MWCNT/AuNPs. In agreement with the experimental results, the computational Monte Carlo and molecular dynamics simulations further supported the highly stabilized GCE/MWCNT/AuNPs-xylitol interactions. It is anticipated that the theoretical and experimental framework developed in this study will be useful for elucidating molecular interactions on nanostructured sensing platforms.

Declaration of Competing Interest

The authors declare that they have no known competing financial interests or personal relationships that could have appeared to influence the work reported in this paper.

Acknowledgments

The authors extend their appreciation to Durban University of Technology for funding and facilities. **KB** also acknowledges the Centre for High Performance Computing (CHPC), Cape Town, South Africa, for all the computational resources.

Supplementary materials

Supplementary material associated with this article can be found, in the online version, at doi:10.1016/j.talo.2022.100144.

References

[1] A.S. Lourenço, F.A. Sanches, R.R. Magalhães, D.J. Costa, W.F. Ribeiro, K. M. Bichinho, G.R. Salazar-Banda, M.C. Araújo, Electrochemical oxidation and electroanalytical determination of xylitol at a boron-doped diamond electrode, Talanta 119 (2014) 509–516.
[2] K. Sreenath, Y.P. Venkatesh, Quantification of xylitol in foods by an indirect competitive immunoassay, J. Agric. Food Chem. 58 (2010) 1240–1246.
[3] S.M. Rajapaksha, K. Gerken, T. Archer, P. Lathan, A.S. Liyanage, D. Mlsna, T. E. Mlsna, Extraction and analysis of xylitol in sugar-free gum samples by GCMS–with direct aqueous injection, J. Anal. Methods Chem. (2019) 2019.
[4] A.G. Coelho, D.P. de Jesus, A simple method for determination of erythritol, maltitol, xylitol, and sorbitol in sugar-free chocolates by capillary electrophoresis with capacitively coupled contactless conductivity detection, Electrophoresis 37 (2016) 2986–2991.
[5] S. Sun, H. Wang, J. Xie, Y. Su, Simultaneous determination of rhamnose, xylitol, arabitol, fructose, glucose, inositol, sucrose, maltose in jujube (Zizyphus jujube Mill.) extract: comparison of HPLC–ELSD, LC–ESI–MS/MS and GC–MS,, Chem. Cent. J. 10 (2016) 1–9.
[6] J.P. Matos, L. Proença, M.I.S. Lopes, I.T. Fonseca, The electrochemical oxidation of xylitol on Pt (1 1 1) in acid medium, J. Electroanal. Chem. 57 (2004) 111–117.
[7] S. Wu, H. Guo, L. Wang, Y. Xin, Y. Cheng, W. Fan, An ultrasensitive electrochemical biosensing platform for fructose and xylitol based on boronic acid-diol recognition, Sens. Actuators B Chem. 245 (2017) 11–17.
[8] Y. Mao, S. Tian, S. Gong, Y. Qin, J. Han, S. Deng, A broad-spectrum sweet taste sensor based on Ni (OH) 2/Ni electrode, Sensors 18 (2018) 2758.
[9] L. Wang, Y. Liu, Y. Chen, Effective electrochemical sensor based on Au nanoparticles decorated carboxylated multi-wall carbon nanotube (AuNPS@ c-MWCNTs) nanocomposites for determination of Dicapthon pesticide in agricultural food, Int. J. Electrochem. Sci. (2021) 16.
[10] E.C. Dreaden, L.A. Austin, M.A. Mackey, M.A. El-Sayed, Size matters: gold nanoparticles in targeted cancer drug delivery, Ther. Deliv. 3 (2012) 457–478.
[11] N.B. Messaoud, M.E. Ghica, C. Dridi, M.B. Ali, C.M. Brett, Electrochemical sensor based on multiwalled carbon nanotube and gold nanoparticle modified electrode for the sensitive detection of bisphenol A, Sens. Actuators B Chem. 253 (2017) 513–522.

[12] J.A. Jenkins, T.J. Wax, J. Zhao, Seed-mediated synthesis of gold nanoparticles of controlled sizes to demonstrate the impact of size on optical properties, J. Chem. Educ. 94 (2017) 1090–1093.
[13] I. Hammami, N.M. Alabdallah, Gold nanoparticles: synthesis properties and applications, J. King Saud. Univ. Sci. 33 (2021), 101560.
[14] K. Nekoueian, M. Amiri, M. Sillanpaa, Carbon paste electrode with Au/Pd/MWCNT nanocomposite for nanomolar determination of timolol, Int. J. Electrochem. Sci 12 (2017) 1612–1624.
[15] S. Mehmood, R. Ciancio, E. Carlino, A.S. Bhatti, Role of Au (NPs) in the enhanced response of Au (NPs)-decorated MWCNT electrochemical biosensor, Int. J. Nanomed. 13 (2018) 2093.
[16] A.A. Chapin, P.R. Rajasekaran, D.N. Quan, L. Hu, J. Herberholz, W.E. Bentley, R. Ghodssi, Electrochemical measurement of serotonin by Au-CNT electrodes fabricated on microporous cell culture membranes, Microsyst. Nanoeng. 6 (2020) 1–13.
[17] T.M. Oliveira, S. Morais, New generation of electrochemical sensors based on multi-walled carbon nanotubes, Appl. Sci. 8 (2018) 1925.
[18] P. Kumar, P. Singh, K. Kumari, S. Mozumdar, R. Chandra, A green approach for the synthesis of gold nanotriangles using aqueous leaf extract of Callistemon viminalis, Mater. Lett. 65 (2011), 595–59.
[19] Y. Sheng, W. Qian, J. Huang, B. Wu, J. Yang, T. Xue, Y. Ge, Y. Wen, Electrochemical detection combined with machine learning for intelligent sensing of maleic hydrazide by using carboxylated PEDOT modified with copper nanoparticles, Microchim. Acta 186 (2019) 1–12.
[20] N. Maleki, S. Kashanian, E. Maleki, M. Nazari, A novel enzyme based biosensor for catechol detection in water samples using artificial neural network, Biochem. Eng. J. 128 (2017) 1–11.
[21] H. Hou, Y. Fan, S. Wang, L. Si, B. Li, Immunomodulatory activity of Alaska pollock hydrolysates obtained by glutamic acid biosensor–Artificial neural network and the identification of its active central fragment, J. Funct. Foods 24 (2016) 37–47.
[22] R.K. Mishra, G.A. Alonso, G. Istamboulie, S. Bhand, J.-L. Marty, Automated flow based biosensor for quantification of binary organophosphates mixture in milk using artificial neural network, Sens. Actuators B Chem. 208 (2015) 228–237.
[23] J. Zupan, J. Gasteiger, Neural Networks in Chemistry and Drug Design, John Wiley & Sons, Inc, 1999.
[24] J. Miller, J. Miller, Statistics and Chemometrics for Analytical Chemistry, Pearson Education Limited, Harlow, 2005, pp. 107–149.
[25] Y. Liu, S. Kim, Y.J. Kim, H. Perumalsamy, S. Lee, E. Hwang, T.H. Yi, Green synthesis of gold nanoparticles using Euphrasia officinalisleaf extract to inhibit lipopolysaccharide-induced inflammation through NF-κB and JAK/STAT pathways in RAW 264.7 macrophages, Int. J. Nanomed. (2019) 2945.
[26] P. Singh, Y.J. Kim, D.C. Yang, A strategic approach for rapid synthesis of gold and silver nanoparticles by Panax ginseng leaves, Artif. Cells Nanomed. Biotechnol. 44 (2016) 1949–1957.
[27] G.W.T.M.J. Frisch, Schlegel, H.B., Scuseria, G.E., Robb, M.A., Cheeseman, J.R., Scalmani, G., Barone, V., Petersson, G.A., Nakatsuji, H., Li, X., Caricato, M., Marenich, A.V., Bloino, J., Janesko, B.G., Gomperts, R., Mennucci, B., Hratchian H. P., Ortiz, J.V., Izmaylov, A.F., Sonnenberg J.L., Williams, D.Y., Ding, F., Lipparini, F., Egidi, F., Goings, J., Peng, B., Petrone, A., Henderson, T., Ranasinghe, D., Zakrzewski, V.G., Gao, J., Rega, N., Zheng, G., Liang, W., Hada, M., Ehara, M., Toyota, K., Fukuda, R., Hasegawa, J., Ishida, M., Nakajima, T., Honda, Y., Kitao, O., Nakai, H., Vreven, T., Throssell, K., Montgomery Jr, J.A., Peralta, J.E., Ogliaro, F., Bearpark, M.J., Heyd, J.J., Brothers, E.N., Kudin, K.N., Staroverov, V.N., Keith, T.A., Kobayashi, R., Normand, J., Raghavachari, K., Rendell, A.P., Burant, J.C., Iyengar, S.S., Tomasi, J., Cossi, M., Millam, J.M., Klene, M., Adamo, C., Cammi, R., Ochterski, J.W., Martin, R.L., Morokuma, K., Farkas, O., Foresman, J.B., Fox, D.J. Fox, Gaussian 09 Revision C. 01. (2016).
[28] P. Bandyopadhyay, A. Karmakar, J. Deb, U. Sarkar, M.M. Seikh, Non-covalent interactions between epinephrine and nitroaromatic compounds: a DFT study, Spectrochim. Acta A Mol. Biomol. 228 (2020), 117827.
[29] D. Biovia, Material Studio modelling. v. 16.1. 0, Dassault Systemes, San Diego, 2016.
[30] G.E. Uwaya, Y. Wen, K. Bisetty, A combined experimental-computational approach for electrocatalytic detection of epinephrine using nanocomposite sensor based on polyaniline/nickel oxide, J. Electroanal. Chem. (2022), 116204.
[31] V. Duc Chinh, G. Speranza, C. Migliaresi, N. Van Chuc, V. Minh Tan, N.T. Phuong, Synthesis of gold nanoparticles decorated with multiwalled carbon nanotubes (Au-MWCNTs) via cysteaminium chloride functionalization, Sci. Rep. 9 (2019) 1–9.
[32] S. Mohan, O.S. Oluwafemi, S.P. Songca, D. Rouxel, P. Miska, F.B. Lewu, N. Kalarikkal, S. Thomas, Completely green synthesis of silver nanoparticle decorated MWCNT and its antibacterial and catalytic properties, *Pure* Appl. Chem. 88 (2016) 71–81.
[33] J.J. Pietrzak, J. Jeszka, Gold nanoparticles grown on multiwall carbon nanotubes, Mater. Sci. Pol. 27 (2009) 693–698.
[34] A.A. Bojang, H.S. Wu, Characterization of electrode performance in enzymatic biofuel cells using cyclic voltammetry and electrochemical impedance spectroscopy, Catalysts 10 (2020) 782.
[35] C. Wang, C. Li, F. Wang, C. Wang, Covalent modification of glassy carbon electrode with L-cysteine for the determination of acetaminophen, Microchim. Acta 155 (2006) 365–371.
[36] E. Laviron, General expression of the linear potential sweep voltammogram in the case of diffusionless electrochemical systems, J. Electroanal. Chem. Interfacial Electrochem. 101 (1979) 19–28.
[37] C. Wu, J. Li, X. Liu, H. Zhang, R. Li, G. Wang, Z. Wang, Q. Li, E. Shangguan, Simultaneous voltammetric determination of epinephrine and acetaminophen using a highly sensitive CoAl-OOH/reduced graphene oxide sensor in pharmaceutical samples and biological fluids, Mater. Sci. Eng. C 119 (2021), 111557.
[38] M.A.S.M. Haniff, S.M. Hafiz, K.A. Wahid, Z. Endut, M.I. Syono, N.M. Huang, S. A. Rahman, I.A. Azid, Nitrogen-doped multiwalled carbon nanotubes decorated with copper (I) oxide nanoparticles with enhanced capacitive properties, J. Mater. Sci. 52 (2017) 6280–6290.
[39] H.D. Dawoud, T. Al Tahtamouni, N. Bensalah, Sputtered manganese oxide thin film on carbon nanotubes sheet as a flexible and binder-free electrode for supercapacitors, Int. J. Energy Res. 43 (2019) 1245–1254.
[40] O.E. Fayemi, A.S. Adekunle, E.E. Ebenso, Metal oxide nanoparticles/multi-walled carbon nanotube nanocomposite modified electrode for the detection of dopamine: comparative electrochemical study, J. Biosens. Bioelectron. 6 (2015), 10.4172.
[41] J.I. Gowda, S.T. Nandibewoor, Electrochemical behavior of paclitaxel and its determination at glassy carbon electrode, Asian J. Pharm. Sci. 9 (2014) 42–49.
[42] A. Kousar, E. Peltola, T. Laurila, Nanostructured geometries strongly affect fouling of carbon electrodes, ACS omega 6 (2021) 26391–26403.
[43] X. Liu, S. You, F. Ma, H. Zhou, Characterization of electrode fouling during electrochemical oxidation of phenolic pollutant, Front. Environ. Sci. Eng. 15 (2021) 1–10.
[44] X. Yang, J. Kirsch, J.W. Fergus, A.L. Simonian, Modeling analysis of electrode fouling due to electro-oxidation of phenols, J. Electrochem. Soc. 140 (1993) 903–911.
[45] O.A. Arodola, S. Kanchi, P. Hloma, K. Bisetty, A.M. Asiri, An in-silico layer-by-layer adsorption study of the interaction between Rebaudioside A and the T1R2 human sweet taste receptor: modelling and biosensing perspectives, Sci. Rep. 10 (2020) 1–18.
[46] G. Uwaya, N.J. Gumede, K. Bisetty, Electrocatalysis of endosulfan based on Fe3O4: an experimental and computational approach, ACS omega 6 (45) (2021) 30515–30525.
[47] B.T. Murti, A.D. Putri, S. Kanchi, M.I. Sabela, K. Bisetty, A.M. Asiri, Light induced DNA-functionalized TiO2 nanocrystalline interface: theoretical and experimental insights towards DNA damage detection, J. Photochem. Photobiol. B Biol. 188 (2018) 159–176.
[48] D. Wang, B. Huang, J. Liu, X. Guo, G. Abudukeyoumu, Y. Zhang, B.C. Ye, Y. Li, A novel electrochemical sensor based on Cu@ Ni/MWCNTs nanocomposite for simultaneous determination of guanine and adenine, Biosens. Bioelectron. 102 (2018) 389–395.